IJICTR
International Journal of Information & Communication Technology Research

Volume 18- Number 2 – 2026 (1-11)

Intelligent Reflecting Surface for Secrecy Rate Enhancement in UAV-Assisted Wireless Powered Communication

Kosar Ansari
Department of Electrical and Computer Engineering
University of Kashan
Kashan, Iran
k.ansari74@grad.kashanu.ac.ir

Mahdi Majidi*
Department of Electrical and Computer Engineering
University of Kashan
Kashan, Iran
m.majidi@kashanu.ac.ir

Received: 11 July 2025 – Revised: 11 October 2025 - Accepted: 11 November 2025

Abstract—**3D beamforming is an advanced beamforming method designed to enhance the performance of wireless communication systems. This paper investigates a wireless-powered communication network incorporating an intelligent reflecting surface (IRS) that employs the 3D beamforming method. The IRS consists of numerous passive reflective elements, each capable of adjusting the phase of the reflected signals. Additionally, a UAV serves as a wireless transmitter to communicate with a ground user via the IRS. An optimization problem is formulated to maximize the secrecy rate by jointly optimizing the UAV's trajectory and the IRS's phase shift configuration. The energy harvesting (EH) of the user, achieved through the simultaneous wireless information and power transfer (SWIPT) method, is incorporated as a constraint. To solve the optimization problem, convexification techniques, such as Taylor expansion, are employed to alternately optimize the solution. Numerical results demonstrate that the use of IRS technology and 3D beamforming enhances EH and significantly improves the secrecy rate.**

Keywords: 3D beamforming; UAV; secrecy rate; wireless powered communication networks; intelligent reflecting surfaces.

Article type: Research Article
© The Author(s).
Publisher: ICT Research Institute

I. INTRODUCTION

The rapid growth in using communication systems has created a demand for new ideas and studies to manage and support the massive number of users. One such innovation in wireless communication is wireless power transfer (WPT) technology. WPT supplies power to the users wirelessly, addressing battery-related challenges such as limited battery life, the inconvenience of carrying heavy batteries, and the risk of running out of battery power by utilizing RF-energy-harvesting (RF-EH) receivers. EH from natural sources such as solar and wind depends on various factors and suffers from severe reliability issues. In contrast, RF signals can deliver energy to EH devices more reliably while simultaneously enabling signal transmission. One of the key EH technologies is WPT, which overcomes many limitations of traditional EH methods. An extension of WPT, simultaneous wireless information and power transfer (SWIPT), allows for the

* Corresponding Author

[Downloaded from ijict.itrc.ac.ir on 2026-11-11]

simultaneous transmission of data and power via the same magnetic or electromagnetic fields [1-4]. In [5], a wireless-powered full-duplex heterogeneous network is considered, and both spectral efficiency and energy efficiency (EE) are studied.

Certainly, power isn't the only challenge in communication. One of the major issues in wireless communication is signal unavailability—In other words, the inability to make calls or access the internet due to the lack of antenna coverage, especially while traveling or in remote areas. However, innovative solutions have been introduced to address this challenge. One promising approach is the use of unmanned aerial vehicles (UAVs). Deploying UAVs in areas with limited or no network coverage can help extend connectivity to users worldwide, even in remote jungles or high-altitude mountainous regions. Moreover, UAVs can facilitate SWIPT, enhancing both communication and energy delivery [6].

Another technology that can enhance communication coverage is the intelligent reflecting surface (IRS). IRS, also referred to as reconfigurable intelligent surface (RIS), has metasurfaces composed of numerous reflecting elements, each capable of adjusting the phase and amplitude of the reflected signal to effectively shape the output beam [7, 8]. Additionally, IRSs can be utilized to enhance both the secrecy rate and WPT [9, 10]. When the objective is to enhance the data rate of the authorized user while concurrently restricting that of the eavesdropper, the secrecy rate can be used as the cost function [11]. In [12], a system with an eavesdropper and two relays is proposed, where the relays re-encode and transmit signals using optimal beamforming to maximize the secrecy rate, while two friendly jammers degrade the eavesdropper’s channel. This paper seeks to improve the secrecy rate. To maximize the network secrecy rate against a full-duplex active eavesdropper, the authors of [13] propose jointly optimizing the base station (BS) beamforming vector and the IRS reflecting elements' phases. Another study, presented in [14], focuses on a simultaneously transmitting and reflecting (STAR)-RIS-assisted secure communication system. The authors propose a joint optimization of the BS's beamforming and the STAR-RIS phase shifts to enhance the secrecy rate under the realistic condition of imperfect channel state information (CSI).

The increasing number of users in wireless communication systems requires advanced methods to manage user connectivity and ensure comprehensive coverage. One of these methods is beamforming, which is traditionally implemented in 2D. However, studying beamforming in 3D offers a more precise approach to handling large-scale communication networks. By integrating 3D beamforming with IRS, there would be greater control over the behavior of the surface, providing additional degrees of freedom for directing signals to user equipment. 3D beamforming is a technique that controls the transmitter's radiation pattern in both the azimuth and elevation planes within a 3D space. This is accomplished by adjusting two key parameters: the tilt and azimuth angles of the transmitter’s antenna array [15]. This capability allows the radiated beam to be steered in any desired direction, thereby improving network performance [16]. The IRS with 3D beamforming capability is proposed for future 6G implementation [17].

There exists an inherent, uncontrollable stochastic variability that contributes to the unreliability of wireless communication systems. To address this, it is essential to understand, model, and mitigate this unpredictability through advanced signal processing techniques at both the transmitter and receiver. The introduction of the IRS and the concept of smart radio environments offers promising solutions to partially control and optimize signal performance [18, 19].

In [20], a system involving a UAV, a source, a user, and an eavesdropper is proposed to study the secrecy rate. In this system, there is no direct link between the source and the user; therefore, the UAV is used to enable communication. The UAV is equipped with 3D beamforming capabilities. However, 3D beamforming consumes a significant amount of energy, and since the UAV’s power is limited due to its reliance on batteries, EH methods like WPT could be utilized. However, these methods may not provide sufficient power for energy-intensive techniques like 3D beamforming, and the UAV trajectory is not considered in this study. In [21], a system with a UAV as the source is examined, where the direct link to the user is blocked, necessitating the use of an IRS as a relay with beamforming capabilities. In addition to beamforming, this research also explores UAV trajectory design. However, it does not address secrecy rate or the possibility of feeding users wirelessly, and it employs traditional 2D beamforming methods.

UAV communications empowered by IRS create a synergistic framework that harnesses the distinct advantages of both technologies, providing an efficient solution for diverse applications envisioned in 6G networks [22]. The authors in [23] employ a UAV-mounted IRS system powered by SWIPT to enhance uplink transmissions, thereby improving EE and prolonging network operation. In [24], a UAV-user communication system with both uplink and downlink transmissions, using an IRS as a relay, is analyzed to improve the secrecy rate and power transfer by optimizing IRS phase shifts and UAV trajectory, but beamforming methods are not discussed. In [25], an Internet of Things (IoT) system with an IRS, UAV, and user is considered, with the main goal of maximizing the secrecy rate while also addressing UAV trajectory design and IRS phase shift optimization. A recent work [26] explores enhancing secrecy rate performance by leveraging an IRS mounted on a UAV, where the optimization jointly considers the UAV's trajectory, the IRS phase configuration, and the transmit power. The work in [27] jointly optimizes UAV trajectory and IRS phase configuration to maximize sum secrecy rate, but further incorporates SWIPT to address EH requirements of ground users. Connecting the IRS to the UAV grants it mobility, providing greater flexibility in positioning itself optimally with respect to the environment and the locations of the BS and users. On the other hand, placing the IRS on the ground allows for larger dimensions, while the UAV benefits from reduced weight, leading to longer flight endurance.

[Downloaded from ijict.itrc.ac.ir on 2026-11-11]

TABLE I. BENCHMARKING OUR IRS SYSTEM WITH PRIOR WORKS.

	[13]	[23]	[24]	[25]	[26]	[27]	This work
BS Location	G	G	U	U	G	G	U
IRS Placement	G	U	G	G	U	U	G
Trajectory Design for U		✓	✓	✓	✓	✓	✓
Secrecy rate	✓		✓	✓	✓	✓	✓
Jammer	✓						
SWIPT		✓				✓	✓

BS: Base station
G: Ground
U: UAV

Our system capabilities are comparatively evaluated against state-of-the-art approaches in Table 1. In this research, the flight of a UAV along with a fixed IRS on the ground utilizing 3D beamforming technology is employed to maximize the secrecy rate for a ground user using SWIPT technology and wirelessly provide energy for it. To achieve this, we define an optimization problem that, when solved, allows for the determination of the optimal UAV flight trajectory and the phase configuration of the IRS. Since the initial problem is not convex, convexification methods are employed to make it convex, and then a convex-based algorithm is presented.

The rest of this paper is organized as follows. Section II describes the system model, which includes the users, IRS, eavesdropper, and UAV. The optimization problem and proposed solution are described in Section III. Section IV presents the numerical results, and Section V concludes the paper.

II. SYSTEM MODEL

As mentioned in the introduction, the system model includes a UAV (U), an IRS (I) with $M = M_x \times M_z$ reflecting elements, a ground user (G), and an eavesdropper (E), which are shown in Fig. 1. There are Line-of-Sight (LoS) and Non-Line-of-Sight (NLoS) paths between the UAV and the IRS, between the IRS and G, and between the IRS and E. Additionally, there are NLOS paths between the UAV and both G and E.

The channels between the UAV and the IRS, the UAV and G, the UAV and E, the IRS and G, and the IRS and E are denoted respectively by $\boldsymbol{h}_{UI} \in C^{1\times M}$, $h_{UG} \in C^{1\times 1}$, $h_{UE} \in C^{1\times 1}$, $\boldsymbol{h}_{IG} \in C^{M\times 1}$, and $\boldsymbol{h}_{IE} \in C^{M\times 1}$. Two angles are essential for 3D beamforming: the azimuth (horizontal) angle and the elevation (vertical) angle. The azimuth angles between the IRS and the UAV, and between the IRS and each $B \in \{G, E, U\}$, are denoted as ϕ_{IG}, ϕ_{IE}, and ϕ_{IU}, respectively. Similarly, the corresponding elevation angles are represented by θ_{IG}, θ_{IE}, and θ_{IU}, respectively. The angular relationships are depicted in Fig. 2 and Fig. 3.

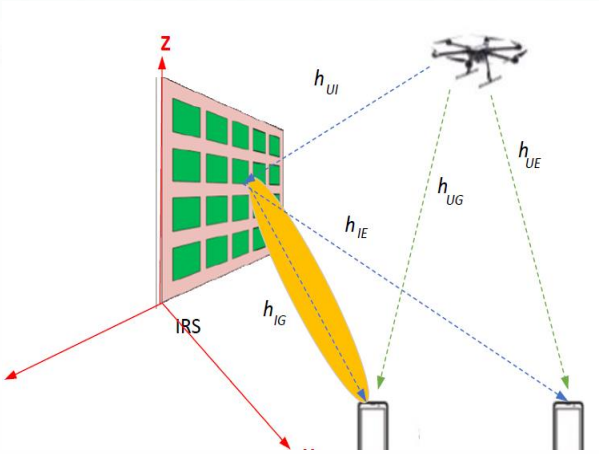

Fig. 1 System model.

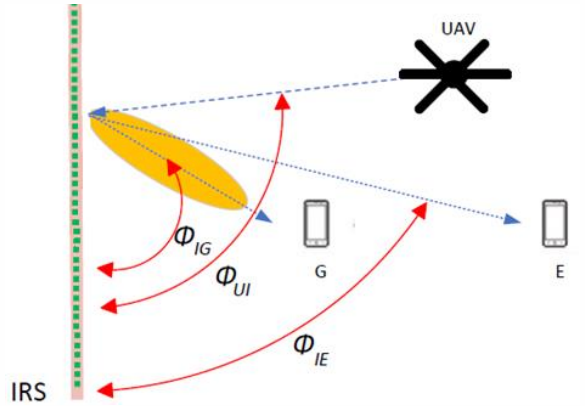

Fig. 2 3D beamforming angles in horizontal angle view. 3D beamforming angles (azimuth and elevation) in the horizontal plane.

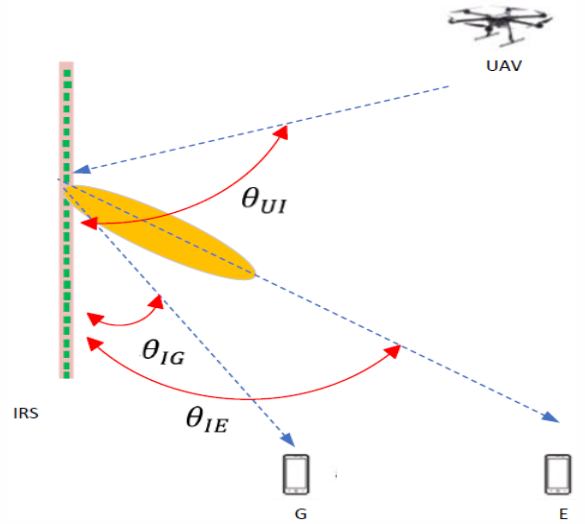

Fig. 3 3D beamforming angles in the vertical plane.

Let $\{x_B, y_B, z_B\}$ represent the 3D coordinates of node $B \in \{G, E, I\}$, while $(x[n], y[n], z_U)$ denotes the UAV's position. The U-G and U-E channel models are given by

$$h_{UG}[n] = \sqrt{\rho d_{UG}^{-k}[n]}\,\tilde{h}_g \qquad (1)$$

[Downloaded from ijict.itrc.ac.ir on 2026-11-11]

$$h_{UE}[n] = \sqrt{\rho d_{UE}^{-k}[n]}\,\tilde{h}_e, \quad (2)$$

where $\tilde{h}_g$ and $\tilde{h}_e$ follow a circularly symmetric complex Gaussian (CSCG) distribution, having a mean of zero and a variance of one. The parameter ρ denotes the path loss at the re ference distance $D_0 = 1\,m$ [28], and k represents the associated path loss exponent. The distances $d_{UE}[n]$ and $d_{UG}[n]$ respectively indicate the separation between U and E, and U and G. The channel gain of the U–I link during the nth time slot follows a Rician distribution and is expressed as [29, 30]

$$\boldsymbol{h}_{UI}[n] = \sqrt{\frac{\beta}{1+\beta}}\,\boldsymbol{h}_{UI}^{LOS}[n] + \sqrt{\frac{1}{\beta+1}}\,\boldsymbol{h}_{UI}^{NLOS}, \quad (3)$$

$$n = 1,2,\dots,N,$$

where

$$\boldsymbol{h}_{UI}^{LOS} = \boldsymbol{a}_y[n] \otimes \boldsymbol{a}_x[n] \quad , n = 1,2,\dots,N, \quad (4)$$

and

$$\boldsymbol{a}_x[n] = \begin{bmatrix} 1, e^{-j\frac{2\pi}{\lambda} d\,\cos(\phi_{UI}[n])\sin(\theta_{UI}[n])}, \dots, \\ e^{-j\frac{2\pi}{\lambda}(M_x-1)d\,\cos(\phi_{UI}[n])\,\sin(\theta_{UI}[n])} \end{bmatrix}^T, \quad (5)$$

$$\boldsymbol{a}_y[n] = \begin{bmatrix} 1, e^{-j\frac{2\pi}{\lambda} d\,\sin(\phi_{UI}[n])\sin(\theta_{UI}[n])}, \dots, \\ e^{-j\frac{2\pi}{\lambda}(M_z-1)d\,\sin(\phi_{UI}[n])\,\sin(\theta_{UI}[n])} \end{bmatrix}^T, \quad (6)$$

$$\sin(\boldsymbol{\phi}_{UI}[n])\,\sin(\boldsymbol{\theta}_{UI}[n]) = \frac{z_U - z_I}{d_{UI}[n]}, \quad (7)$$

$$\cos(\boldsymbol{\phi}_{UI}[n])\,\sin(\boldsymbol{\theta}_{UI}[n]) = \frac{x_I - x[n]}{d_{UI}[n]}, \quad (8)$$

where β denotes the Rician factor, $\otimes$ represents the Kronecker product [30], $d_{UI}[n]$ is the UAV-IRS distance in the nth time slot, and λ is the carrier wavelength.$\boldsymbol{h}_{UI}[n]$ is a complex and non-convex function of $d_{UI}[n]$. Since the UAV operates at a high altitude, the existence of a LoS component in addition to scattered multipath signals—resulting in a Rician fading channel—is a reasonable assumption.

The distance between two neighboring elements of IRS is denoted by d, which is defined as $d = \lambda/2$, and also, $\boldsymbol{h}_{IG}^{NLOS}$ and h_{IE}^{NLOS} are modeled as CSCG random variables, such that their distribution is $\mathcal{CN}(0,1)$. The channel gain for the small-scale fading experienced on the I-G and I-E communication links can be generated using a similar procedure. In addition, the channel gain of the I-G link can be expressed as

$$\boldsymbol{h}_{IG} = \left[|h_{IG,1}|e^{j\omega_{IG,1}}, |h_{IG,2}|e^{j\omega_{IG,2}}, \dots, |h_{IG,M}|e^{j\omega_{IG,M}}\right]^T, \quad (9)$$

where for the ith element of the complex vector $\boldsymbol{h}_{IG}$, $|h_{IG,i}|$ defines its magnitude and $\omega_{IG,i} \epsilon\, [0,2\pi)$ defines its phase angle. $\boldsymbol{h}_{IE}$ and $\boldsymbol{h}_{UI}$ are expressed similarly, and $h_{UG}[n]$ is given by

$$h_{UG}[n] = |h_{UG}[n]|\, e^{j\omega_{UG}[n]}, \quad (10)$$

where $\omega_{UG}[n] \epsilon\, [0,2\pi)$ is the phase angle of the complex vector $h_{UG}[n]$ in the nth time slot.

The path loss of the NLOS path for G and E is defined as

$$L_{UIG}[n] = \sqrt{\rho(d_{IG}\, d_{UI}[n])^{-\alpha}}, \quad (11)$$

$$L_{UIE}[n] = \sqrt{\rho(d_{IE}\, d_{UI}[n])^{-\alpha}}, \quad (12)$$

where α is the path loss exponent [24]. This work adopts the power splitting approach, where a fraction μ of the received signal is allocated to information decoding (ID), and the remaining fraction $1-\mu$ is used for EH, with $0 < \mu < 1$. Based on the aforementioned system model and assuming $E(S^2) = P$, the signal-to-noise ratios (SNRs) at G and E in the nth time slot are given by:

$$\gamma_G[n] = \frac{P\mu|L_{UIG}[n]\,\boldsymbol{h}_{IG}^H\,\Psi[n]\,\boldsymbol{h}_{UI}[n] + h_{UG}[n]|^2}{\sigma^2}, \quad (13)$$

$$\gamma_E[n] = \frac{P|L_{UIE}[n]\,\boldsymbol{h}_{IE}^H\,\Psi[n]\,\boldsymbol{h}_{UI}[n] + h_{UE}[n]|^2}{\sigma^2}, \quad (14)$$

where σ^2 is the noise variance, the phase-shift matrix of IRS in the nth time slot is denoted by $\Psi[n] = \mathrm{diag}\{\psi_1[n], \psi_2[n], \dots, \psi_M[n]\}$, and $(\,)^H$ denotes complex conjugate transpose. The achievable rates of G and E are written as

$$R_G[n] = \log_2(1+\gamma_G[n]) \quad (15)$$

$$R_E[n] = \log_2(1+\gamma_E[n]) \quad (16)$$

III. Problem Formulation and Proposed Optimization

The secrecy rate of the system at time slot n is given by

$$R_{SEC}[n] = R_G[n] - R_E[n], \quad (17)$$

and the total harvested energy at G is expressed as

[Downloaded from ijict.itrc.ac.ir on 2026-11-11]

$$E_H = \sum_{n=1}^{N} \zeta(1-\mu)P\,\delta_t |L_{UIG}[n]\,\boldsymbol{h}_{IG}^H\,\Psi[n]\,\boldsymbol{h}_{UI}[n] + h_{UG}[n]|^2, \tag{18}$$

where $\zeta \in (0,1)$ denotes the EH efficiency factor for G and δ_t is the time step.

The optimization problem for this system model, denoted as P1 below, aims to maximize the secrecy rate while simultaneously satisfying EH constraints, designing the IRS phase-shift matrix, and optimizing the UAV trajectory.

$$\text{P1:} \max_{\psi_i[n],\boldsymbol{q}[n]} \frac{1}{N}\sum_{n=1}^{N} R_{SEC}[n] \tag{19}$$

$$S.T. \quad 0 \le \psi_i[n] \le 2\pi, \quad 1 \le n \le N, \quad 1 \le i \le M \tag{20}$$

$$\|\boldsymbol{q}[n+1] - \boldsymbol{q}[n]\|^2 \le D^2, \quad n = 1,2,\dots,N-1 \tag{21}$$

$$\|\boldsymbol{q}[N] - \boldsymbol{q}_F\|^2 \le 1, \quad \boldsymbol{q}[1] = \boldsymbol{q}_0 \tag{22}$$

$$E_H \ge \underline{E}_H, \tag{23}$$

where $\underline{E}_H$ is the minimum required energy harvested by G, $\boldsymbol{q}[n] = (x[n], y[n])^{\mathrm{T}}$ represents the UAV's 2D position vector at time slot n, $\boldsymbol{q}_0$ and $\boldsymbol{q}_F$ denote the initial and final horizontal waypoints of the UAV trajectory, respectively. Additionally, the maximum horizontal distance achievable by the UAV in a single time slot δ_t is $D = \delta_t V_{MAX}$, while V_{MAX} specifies the UAV's maximum speed. When the two expressions in (13) have identical phases, i.e.,

$$-\omega_{IG,i} + \psi_i[n] + \omega_{UI,i}[n] = \arg(\tilde{h}_g) \quad \forall n, i = 1,2,\dots,M \tag{24}$$

The optimal IRS phase shift can be derived as

$$\psi_i[n] = \omega_{IG,i} - \omega_{UI,i}[n] + \arg(\tilde{h}_g) \quad \forall n, i = 1,2,\dots,M. \tag{25}$$

Therefore, the first term in the SNR expression for G in (13) can be written as

$$L_{UIG}[n]\,\boldsymbol{h}_{IG}^H\,\Psi[n]\boldsymbol{h}_{UI}[n] = \frac{\sqrt{\rho}}{(d_{UI}[n]\,d_{IG})^{\frac{\alpha}{2}}}\sum_{i=1}^{M}|\boldsymbol{h}_{UI,i}[n]|\,|\boldsymbol{h}_{IG,i}|\,e^{j\arg(\tilde{h}_g)}, \tag{26}$$

and accordingly, the SNR of G is obtained as follows

$$\gamma_G[n] = \frac{P\mu}{\sigma^2}\left|\sum_{i=1}^{M}\frac{\sqrt{\rho}}{(d_{UI}[n]\,d_{IG})^{\frac{\alpha}{2}}}|\boldsymbol{h}_{UI,i}[n]|\,|\boldsymbol{h}_{IG,i}| + \sqrt{\rho}\,|\tilde{h}_g|\,d_{UG}^{-\frac{k}{2}}[n]\right|^2. \tag{27}$$

To simplify the analysis and obtain an upper bound for the E's SNR, we assume that the phases of both numerator terms in (14) are aligned too, and we have

$$L_{UIE}[n]\,\boldsymbol{h}_{IE}^H\,\Psi[n]\,\boldsymbol{h}_{UI}[n] = \frac{\sqrt{\rho}}{(d_{UI}[n]\,d_{IE})^{\frac{\alpha}{2}}}\sum_{i=1}^{M}|\boldsymbol{h}_{UI,i}[n]|\,|\boldsymbol{h}_{IE,i}|\,e^{j\arg(\tilde{h}_e)}, \tag{28}$$

hence, the E's SNR can be obtained as

$$\gamma_E[n] = \frac{P}{\sigma^2}\left|\sum_{i=1}^{M}\frac{\sqrt{\rho}}{(d_{UI}[n]\,d_{IE})^{\frac{\alpha}{2}}}|\boldsymbol{h}_{UI,i}[n]|\,|\boldsymbol{h}_{IE,i}| + \sqrt{\rho}\,|\tilde{h}_e|\,d_{UE}^{-\frac{k}{2}}[n]\right|^2 \tag{29}$$

According to the phase alignment, E_H at G is given by

$$E_H = \sum_{n=1}^{N}\zeta(1-\mu)\,P\delta_t\left|\frac{\sqrt{\rho}}{(d_{UI}[n]\,d_{IG})^{\frac{\alpha}{2}}}\sum_{i=1}^{M}|\boldsymbol{h}_{UI,i}[n]|\,|\boldsymbol{h}_{IG,i}| + \sqrt{\rho}\,|\tilde{h}_g|\,d_{UG}^{-\frac{k}{2}}[n]\right|^2, \tag{30}$$

It is assumed that

$$A = \sqrt{\rho}\,|\tilde{h}_g|, \tag{31}$$

$$B[n] = \frac{\sqrt{\rho}}{d_{IG}^{\frac{\alpha}{2}}}\sum_{i=1}^{M}|\boldsymbol{h}_{UI,i}[n]|\,|\boldsymbol{h}_{IG,i}|, \tag{32}$$

$$C = \sqrt{\rho}\,|\tilde{h}_e| \tag{33}$$

$$D[n] = \frac{\sqrt{\rho}}{d_{IE}^{\frac{\alpha}{2}}}\sum_{i=1}^{M}|\boldsymbol{h}_{UI,i}[n]|\,|\boldsymbol{h}_{IE,i}|, \tag{34}$$

$$\gamma_0 = \frac{P}{\sigma^2} \tag{35}$$

$$\gamma_{E_H} = \zeta(1-\mu)P\delta_t, \tag{36}$$

According to the above definitions, the optimization problem can be rewritten as

$$\text{P2:} \max_{\boldsymbol{q},u[n],v[n],z[n]} \frac{1}{N}\sum_{n=1}^{N}\left(\log_2\left[1 + \gamma_0\mu\left|\frac{A}{(d_{UG}[n])^{\frac{k}{2}}} + \frac{B[n]}{(d_{UI}[n])^{\frac{\alpha}{2}}}\right|^2\right]\right.$$

[Downloaded from ijict.itrc.ac.ir on 2026-11-11]

$$-\left[1+\gamma_0\left|\frac{C}{(d_{UE}[n])^{\frac{k}{2}}}+\frac{D[n]}{(d_{UI}[n])^{\frac{\alpha}{2}}}\right|^2\right]) \quad (37)$$

$$S.T.\ d_{UG}[n]\le u[n],\ \ n=1,\dots,N-1 \quad (38)$$

$$d_{UI}[n]\le v[n],\qquad n=1,\dots,N-1 \quad (39)$$

$$d_{UE}[n]\ge z[n],\qquad n=1,\dots,N-1 \quad (40)$$

$$\|\boldsymbol{q}[N]-\boldsymbol{q}_F\|^2\le 1, \boldsymbol{q}[1]=\boldsymbol{q}_0, \quad (41)$$

$$E_H\ge \underline{E_H} \quad (42)$$

where $u[n]$, $v[n]$, and $z[n]$ are auxil iary variables, and E_H is rewritten as

$$E_H=\sum_{n=1}^{N}\zeta(1-\mu)\,P\delta_t\left|\frac{A}{(d_{UG}[n])^{\frac{k}{2}}}+\frac{B[n]}{(d_{UI}[n])^{\frac{\alpha}{2}}}\right|^2. \quad (43)$$

According to [31], assuming that the domain of the function f, denoted as $\mathrm{dom}(f)$, is convex and that $f(\boldsymbol{x})$ is differentiable, provided that $f(\boldsymbol{x})$ is convex, the inequality below holds.

$$f(\mathbf{y})\ge f(\boldsymbol{x})+\nabla f(\boldsymbol{x})^T(\mathbf{y}-\boldsymbol{x})\quad \forall \boldsymbol{x},\mathbf{y}\in \mathrm{dom}(f). \quad (44)$$

Based on the first-order Taylor expansion, the first and second components of the objective function are defined as follows

$$f(u[n],v[n])=[1+\gamma_0\mu\left(\frac{A^2}{u^k[n]}+\frac{B[n]^2}{v^\alpha[n]}+\frac{2A\,B[n]}{u^{\frac{k}{2}}[n]\,v^{\frac{\alpha}{2}}[n]}\right)]$$
$$\simeq A_0[n]+\frac{B_0[n]}{A_0[n]ln2}(u[n]-u_0[n])+\frac{F_0[n]}{A_0[n]\,ln2}(v[n]-v_0[n]), \quad (45)$$

$$f(z[n],v[n])=\left[1+\gamma_0\left(\frac{C^2}{z^k[n]}+\frac{D[n]^2}{v^\alpha[n]}+\frac{2C\,D[n]}{z^{\frac{k}{2}}[n]\,v^{\frac{\alpha}{2}}[n]}\right)\right]$$
$$\simeq C_0[n]+\frac{D_0[n]}{C_0[n]ln2}(z[n]-z_0[n])+\frac{H_0[n]}{C_0[n]\,ln2}(v[n]-v_0[n]), \quad (46)$$

$$f_{E_H}(u[n],v[n])=\gamma_{E_H}\left(\frac{A^2}{u^k[n]}+\frac{B[n]^2}{v^\alpha[n]}+\frac{2A\,B[n]}{u^{\frac{k}{2}}[n]\,v^{\frac{\alpha}{2}}[n]}\right)]$$
$$\simeq A_{E_H}[n]+B_{E_H}[n](u[n]-u_0[n])+C_{E_H}[n](v[n]-v_0[n]), \quad (47)$$

where

$$A_0[n]=1+\gamma_0\mu\left(\frac{A^2}{u_0^k[n]}+\frac{B[n]^2}{v_0^\alpha[n]}+\frac{2A\,B[n]}{u_0^{\frac{k}{2}}[n]v_0^{\frac{\alpha}{2}}[n]}\right), \quad (48)$$

$$B_0[n]=-\gamma_0\mu\left(\frac{kA^2}{(u_0[n])^{k+1}}+\frac{kA\,B[n]}{(u_0[n])^{\frac{k}{2}+1}v_0^{\frac{\alpha}{2}}[n]}\right), \quad (49)$$

$$F_0[n]=-\gamma_0\mu\left(\frac{\alpha\,B[n]^2}{v_0^{\alpha+1}[n]}+\frac{\alpha A\,B[n]}{(u_0[n])^{\frac{k}{2}}v_0^{\frac{\alpha}{2}+1}[n]}\right), \quad (50)$$

$$C_0[n]=1+\gamma_0\left(\frac{C^2}{z_0^k[n]}+\frac{D[n]^2}{v_0^\alpha[n]}+\frac{2C\,D[n]}{z_0^{\frac{k}{2}}[n]v_0^{\frac{\alpha}{2}}[n]}\right), \quad (51)$$

$$D_0[n]=-\gamma_0\left(\frac{kC^2}{(z_0[n])^{k+1}}+\frac{kC\,D[n]}{(z_0[n])^{\frac{k}{2}+1}v_0^{\frac{\alpha}{2}}[n]}\right) \quad (52)$$

$$A_{E_H}[n]=\gamma_{E_H}\left(\frac{A^2}{u_0^k[n]}+\frac{B[n]^2}{v_0^\alpha[n]}+\frac{2A\,B[n]}{u_0^{\frac{k}{2}}[n]v_0^{\frac{\alpha}{2}}[n]}\right), \quad (53)$$

$$B_{E_H}[n]=-\gamma_{E_H}\left(\frac{kA^2}{(u_0[n])^{k+1}}+\frac{kA\,B[n]}{(u_0[n])^{\frac{k}{2}+1}v_0^{\frac{\alpha}{2}}[n]}\right), \quad (54)$$

[Downloaded from ijict.itrc.ac.ir on 2026-11-11]

$$C_{E_H}[n] = -\gamma_{E_H}\left(\frac{\alpha\, B[n]^2}{v_0^{\alpha+1}[n]} + \frac{\alpha A\, B[n]}{(u_0[n])^{\frac{k}{2}} v_0^{\frac{\alpha}{2}+1}[n]}\right). \quad (55)$$

Furthermore, by applying the first-order Taylor series approximation, the following inequalities are derived.

$$-u^2[n] \le u_0^2[n] - 2u_0[n]u[n], \quad (56)$$

$$-v^2[n] \le v_0^2[n] - 2v_0[n]v[n], \quad (57)$$

Additionally, the squared distance between the UAV and E at time slot *n* is given by

$$d_{UE}^2[n] = \|\boldsymbol{q}[n] - \boldsymbol{W}_E\|^2 + \|Z_U - Z_E\|^2, \quad (58)$$

where $\boldsymbol{W}_E$ denotes the horizontal coordinates of E, and Z_U and Z_E represent the altitudes of the UAV and E, respectively.

$$\|\boldsymbol{q}[n] - \boldsymbol{W}_E\|^2 = (\boldsymbol{q}[n] - \boldsymbol{W}_E)^T(\boldsymbol{q}[n] - \boldsymbol{W}_E), \quad (59)$$

$$(\boldsymbol{q}[n] - \boldsymbol{W}_E)^T(\boldsymbol{q}[n] - \boldsymbol{W}_E) = \boldsymbol{q}^T[n]\,\boldsymbol{q}[n] - \boldsymbol{q}[n]^T\boldsymbol{W}_E - \boldsymbol{W}_E^T\boldsymbol{q}[n] + \boldsymbol{W}_E^T\boldsymbol{W}_E, \quad (60)$$

The Taylor series expansion of a term in equation (60) is approximated as

$$\boldsymbol{q}^T[n]\,\boldsymbol{q}[n] \simeq \boldsymbol{Q}_0^T[n]\,\boldsymbol{Q}_0[n] + 2\boldsymbol{Q}_0^T[n](\boldsymbol{q}[n] - \boldsymbol{Q}_0[n]) \quad (61)$$

where $\boldsymbol{Q}_0[n]$ denotes the initial UAV trajectory. The resulting expression is an affine function of $\boldsymbol{q}[n]$.

According to (59) and (60), (40) is rewritten as

$$(2\boldsymbol{Q}_0^T[n]\boldsymbol{q}[n] - \boldsymbol{q}[n]^T\boldsymbol{W}_E - \boldsymbol{W}_E^T\boldsymbol{q}[n] + \boldsymbol{W}_E^T\boldsymbol{W}_E) + \|Z_U - Z_E\|^2 \ge z^2[n] \quad ,\forall n, \quad (62)$$

As a result, the final problem is formulated as

$$\text{P3:} \max_{\boldsymbol{q},u[n],v[n],z[n]} \frac{1}{N}\sum_{n=1}^{N}\left[\left(\frac{B_0[n]}{A_0[n]\,ln2}u[n] + \frac{F_0[n]}{A_0[n]\,ln2}\,v[n]\right) - \left(\frac{D_0[n]}{C_0[n]\,ln2}z[n] + \frac{H_0[n]}{C_0[n]\,ln2}v[n]\right)\right] \quad (63)$$

$$S.T.\ \ (d_{UG}[n])^2 + u_0^2[n] - 2u_0[n]\,u[n] \le 0\,, \forall n \quad (64)$$

$$(d_{UR}[n])^2 + v_0^2[n] - 2v_0[n]\,v[n] \le 0, \forall n \quad (65)$$

$$z^2[n] - 2\boldsymbol{Q}_0^T[n]\boldsymbol{q}[n] + \boldsymbol{q}[n]^T\boldsymbol{W}_E + \boldsymbol{W}_E^T\boldsymbol{q}[n] - \boldsymbol{W}_E^T\boldsymbol{W}_E + \|Z_U - Z_E\|^2] \le 0, \quad \forall n \quad (66)$$

$$\|\boldsymbol{q}[N] - \boldsymbol{q}_F\|^2 \le 1, \boldsymbol{q}[1] = \boldsymbol{q}_0 \quad (67)$$

$$\|\boldsymbol{q}[n+1] - \boldsymbol{q}[n]\|^2 \le D^2, \forall n \quad (68)$$

$$\sum_{n=1}^{N}\big(A_{E_H}[n] + B_{E_H}[n](u[n] - u_0[n]) + C_{E_H}[n](v[n] - v_0[n])\big) \ge \underline{E}\,. \quad (69)$$

The convex nature of Problem P3 enables its efficient solution through CVX in MATLAB. Algorithm 1 outlines the steps for solving P3.

Algorithm 1 for solving problem P3

1: **Initialization:** set initial variables ($\boldsymbol{Q}_0[n]$, $u_0[n], v_0[n]$, $z_0[n]$ and ϵ) and (R_{SEC_0}) is obtained by $\boldsymbol{Q}_0[n]$, (13) ,(14), (15), (16) and (17), *k*=0.
2: Compute $A, B_0[n], C$, and $D_0[n]$ with the given above parameters.
3: Repeat
4: Set $k \leftarrow k+1$.
5: With solving P3, update $\boldsymbol{q}_k$, u_k, v_k, and z_k.
6: By calculating (3), (13), (14), (15), (16) and (17) update $\boldsymbol{q_k}[n], u_k[n], v_k[n]$, and $z_k[n]$, also R_{SEC_k} and $\boldsymbol{h}_{UI_k}$.
7: With given $R_{SEC_k}[n]$ and $h_{UI_k}[n]$, update $B_k[n]$ and $D_k[n]$.
8: Set $u_0[n] = u_k[n], v_0[n] = v_k[n]$, $z_0[n]$= $z_k[n]$, and $\boldsymbol{Q}_0[n] = \boldsymbol{q_k}[n]$.
9: Until: $\left|\frac{R_{SEC_k} - R_{SEC_{k-1}}}{R_{SEC_k}}\right| < \epsilon$.
10: Output: { $\boldsymbol{q}[n]$ }, $n = 1, \dots, N-1$

Each iteration of Algorithm 1 requires solving convex Problem P3 once using interior-point methods. In this problem, the number of optimization variables is $N(3+3d_q)$, where d_q denotes the dimensionality of $\boldsymbol{q}[n]$ ($d_q = 2$ for 2D trajectories), resulting in $9N$ variables. The number of constraints is $4N+3$, which also scales linearly with N. Since the computational complexity of interior-point methods typically scales cubically with the number of variables, the per-iteration

[Downloaded from ijict.itrc.ac.ir on 2026-11-11]

complexity of Algorithm 1 is $\mathcal{O}(N^3)$. Considering that Algorithm 1 requires $I_{\max}$ iterations to converge, the total computational complexity is $\mathcal{O}(I_{max}N^3)$. The alternating optimization loop typically converges in $\mathcal{O}(\log(1/\epsilon))$ iterations where ϵ is the convergence threshold for the stopping criterion.

TABLE II. SIMULATION PARAMETERS.

Symbol	Description	Value
κ	Path loss exponent of U-G and U-E links	3.5
α	Path loss exponent of U-I-G and U-I-E links	2.2
$\boldsymbol{q}_0$	Initial horizontal waypoint of the UAV (U)	$[-200,10]^T$m
$\boldsymbol{q}_F$	Final horizontal waypoint of U	$[200,10]^T$m
$\boldsymbol{W}_G$	Horizontal coordinates of the ground user (G)	$[0,70]^T$ m
$\boldsymbol{W}_I$	Horizontal coordinates of the IRS (I)	$[0,0]^T m$
$\boldsymbol{W}_E$	Horizontal coordinates of the eavesdropper (E)	$[100,50]^T$m
Z_U	Height of U above the ground	80 m
Z_G	Height of G above the ground	0 m
Z_I	Height of I above the ground	40 m
Z_E	Height of E above the ground	0 m
V_{MAX}	Maximum velocity of U	25 m/s
δ_t	Time step	5 s
σ^2	Noise variance	−80 dBm
P	Transmission power at U	1 W
β	Rician factor	2
ρ	Path loss at the reference distance $D_0 = 1\ m$	−20 dB
λ	Carrier wavelength	1
T	Total flight time	800 s
ζ	EH efficiency factor	0.5
$\underline{E}$	Minimum required energy harvested by G	10^{-6} J
μ	Fraction μ of received signal allocated to ID; remaining fraction (1−μ) used for EH	0.7
M_x	Number of IRS elements along the x-axis	6
M_z	Number of IRS elements along the z-axis	5
M	Total number of IRS reflecting elements ($M = M_x \times M_z$)	30
ϵ	Convergence threshold for the stopping criterion in Algorithm 1	10^{-4}

IV. NUMERICAL RESULTS

This section presents simulation results examining the UAV trajectory, IRS phase-shift design, and EH performance in the context of secrecy rate maximization. For comparati ve evaluation, we implement the following benchmark approaches:

T/NPB: UAV trajectory (T) design with no (IRS) passive beamforming (NPB).

JT/PB: Joint UAV trajectory (JT) design and IRS passive beamforming (PB).

HT/PB: Heuristic UAV trajectory (HT) with IRS passive beamforming.

The selected system parameters used in the simulations are summarized in Table 2, together with their short descriptions for clarity.

In the heuristic trajectory (denoted by HT) approach, the UAV initiates its flight from the starting point, traveling at the maximum speed V_{MAX} until it reaches the airspace directly above user G. Upon arrival, it enters a stationary hovering phase for a predetermined duration, after which it resumes travel at the same constant speed V_{MAX} toward the final destination. This complete trajectory profile is illustrated in Fig. 4 using X-Y coordinates.

Fig. 4 illustrates the UAV trajectory under three different modes. In the JT/PB mode, the UAV is shown hovering between G and the IRS to maximize the average secrecy rate. A comparison between JT/PB and T/NPB modes reveals that maintaining a shorter distance from the IRS plays a significant role in achieving higher secrecy rates. Furthermore, as secrecy rate maximization is the primary objective, the JT/PB trajectory remains closer to the user's location than to the IRS. Additionally, since secrecy rate optimization is prioritized while EH is treated as a constraint, the UAV, after getting close to the user's location horizontally, attempts to maintain a safe distance from E, as also depicted in Fig. 4.

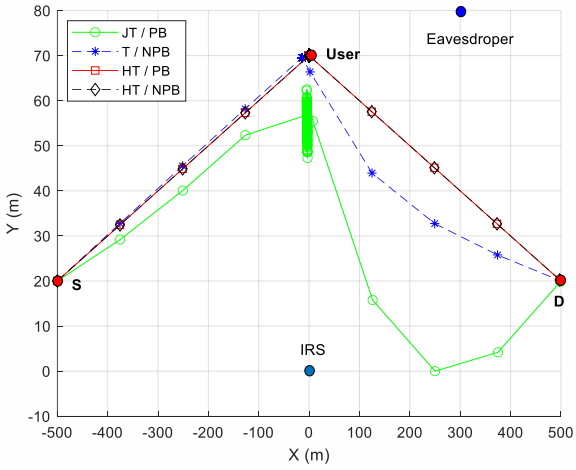

Fig. 4 UAV trajectory in JT/PB, T/NPB, HT/PB, and HT/PB.

[Downloaded from ijict.itrc.ac.ir on 2026-11-11]

Regarding the practical runtime, the complete optimization process — including IRS phase-shift calculation and UAV trajectory design via Algorithm 1 — required approximately 50 seconds for the JT/PB method results presented in Fig. 4 .All computations were performed in MATLAB using CVX with the SDPT3 solver on a computing platform equipped with an Intel Core i7-8550U CPU (1.80 GHz base frequency, up to 1.99 GHz turbo) and 8 GB of DDR4 RAM.

While Fig. 4 plots the UAV trajectory as discrete (x,y) points, it does not clearly represent temporal variations during hovering phases. To better visualize the time-dependent positional changes, we provide complementary 2D projections in Fig. 5 (vertical plane) and Fig. 6 (horizontal plane), derived from the same trajectory data as Fig. 4 .These figures compare the JT/PB and HT/PB schemes. While the HT/PB trajectory follows a predetermined heuristic path, the JT/PB trajectory is optimally derived through Algorithm 1. As observed in the optimized trajectory, after approaching the user's horizontal location, the UAV hovers there for most of the time (depending on the total flight duration) and subsequently proceeds to its final destination.

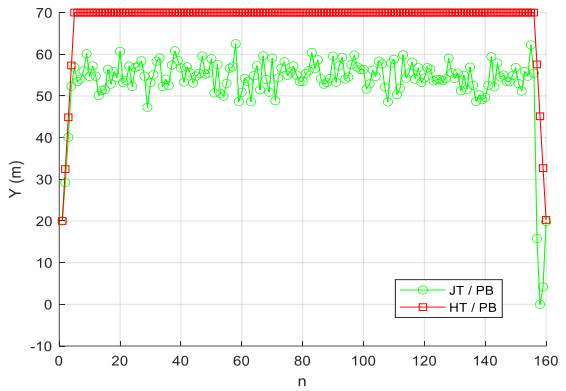

Fig. 5 UAV trajectory from a vertical perspective.

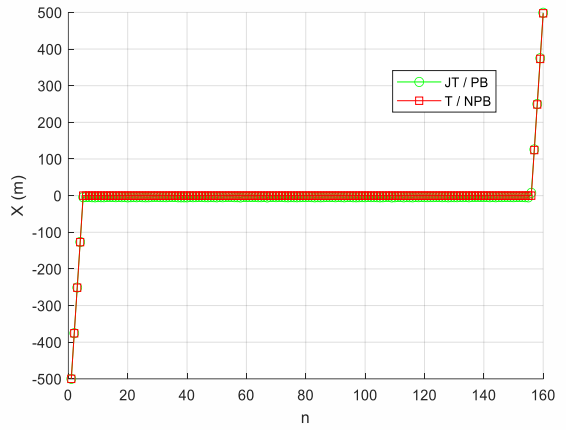

Fig. 6 UAV trajectory from a horizontal perspective.

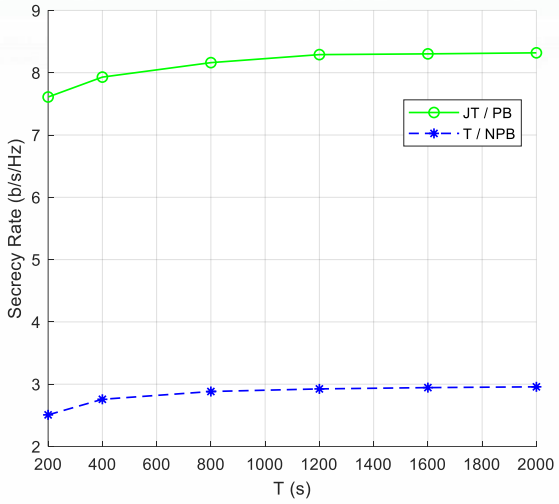

Fig. 7 Secrecy rate versus flight duration in JT/PB and T/NPB modes.

Fig. 7 presents the variation of the secrecy rate with respect to the UAV's total flight time ($T = N\delta_t$) for both JT/PB and T/NPB modes. The findings indicate that integrating IRS under JT/PB mode yields more than twice the secrecy rate compared to the T/NPB approach. This significant improvement arises from the optimal configuration of each IRS element's phase, which ensures that the reflected signal at G is coherently aligned with the direct signal from U. This constructive interference introduces M additional signal paths, leading to stronger received power and an enhanced SNR at the legitimate receiver (G). Meanwhile, due to the destructive interference resulting from the optimized IRS phases, natural beamforming nulls are formed toward E, effectively suppressing the eavesdropper's signal. Furthermore, as T increases, the UAV benefits from extended hovering at the point that exhibits the maximum secrecy rate—for instance, in JT/PB mode, this optimal point lies between the IRS and the user, as depicted in Fig. 4.

Fig. 8 demonstrates a consistent performance gap between the JT/PB and HT/PB schemes across different IRS sizes (M). As observed in subfigure (a), the JT/PB scheme achieves a higher secrecy rate. This is a direct result of its optimized trajectory, which is explicitly designed to maximize secrecy, whereas the HT/PB scheme follows a predetermined heuristic path that does not prioritize this objective. In contrast, subfigure (b) reveals that the HT/PB scheme yields a higher EH performance. This outcome is attributed to its trajectory, which positions the UAV closer to the IRS for prolonged periods, thereby enhancing the energy transfer efficiency. This design choice, however, creates a fundamental trade-off, as the gain in EH comes at the expense of a lower secrecy rate. It is also important to note that the EH for both schemes satisfies the minimum constraint defined in the optimization problem ($\underline{E}$). Furthermore, according to (18), a smaller value of the parameter μ leads to higher EH.

[Downloaded from ijict.itrc.ac.ir on 2026-11-11]

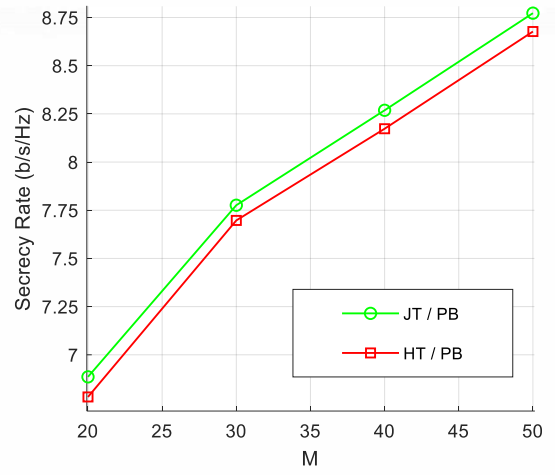

(a)

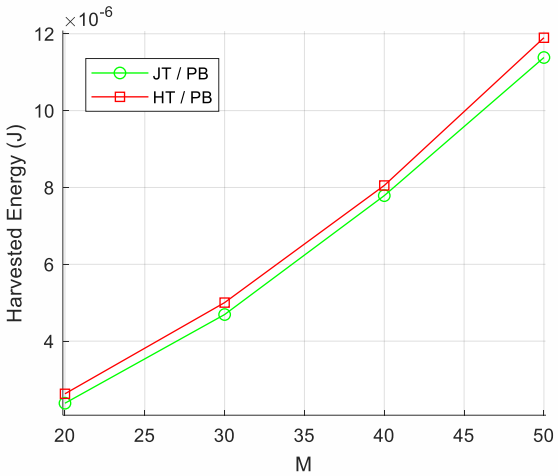

(b)

Fig. 8 Effect of the number of IRS elements (M) on the performance of the JT/PB and HT/PB schemes (μ=0.3): (a) Secrecy Rate; (b) Harvested Energy.

V. Conclusion

In this paper, we investigated a wireless communication system that integrates 3D beamforming and an IRS to enhance the secrecy rate. A UAV was employed to transmit information to the user while also supporting simultaneous EH. We formulated and solved an optimization problem to jointly design the UAV's trajectory and the IRS phase shifts, aiming to maximize the secrecy rate under EH constraints. Numerical results demonstrated that the integration of 3D beamforming and IRS significantly improves both communication security and EH performance. These results highlight the potential of IRS-assisted systems in the design of future secure and energy-efficient wireless networks.

References

[1] S. Bi, C. K. Ho, and R. Zhang, "Wireless powered communication: Opportunities and challenges," *IEEE Communications Magazine*, vol. 53, no. 4, pp. 117-125, 2015.

[2] Z. Ding *et al.*, "Application of smart antenna technologies in simultaneous wireless information and power transfer," *IEEE Communications Magazine*, vol. 53, no. 4, pp. 86-93, 2015.

[3] D. W. K. Ng, E. S. Lo, and R. Schober, "Energy-efficient resource allocation in OFDMA systems with hybrid energy harvesting base station," *IEEE Transactions on Wireless Communications*, vol. 12, no. 7, pp. 3412-3427, 2013.

[4] L. R. Varshney, "Transporting information and energy simultaneously," in *IEEE international symposium on information theory*, 2008: IEEE, pp. 1612-1616.

[5] S. Haghgoy, M. Mohammadi, and Z. Mobini, "Spectral and energy efficiency wireless-powered massive-MIMO heterogeneous network," *International Journal of Information and Communication Technology Research*, vol. 14, no. 1, pp. 13-24, 2022.

[6] Y. Zeng, R. Zhang, and T. J. Lim, "Wireless communications with unmanned aerial vehicles: Opportunities and challenges," *IEEE Communications Magazine*, vol. 54, no. 5, pp. 36-42, 2016.

[7] M. A. ElMossallamy, H. Zhang, L. Song, K. G. Seddik, Z. Han, and G. Y. Li, "Reconfigurable intelligent surfaces for wireless communications: Principles, challenges, and opportunities," *IEEE Transactions on Cognitive Communications and Networking*, vol. 6, no. 3, pp. 990-1002, 2020.

[8] F. Ghalgarzadeh, M. Majidi, and R. Mirzavand, "Phase shift design for intelligent reflecting surfaces under practical reflection models in NOMA network," presented at the 8th Iranian Conference on Signal Processing and Intelligent Systems (ICSPIS), 2022.

[9] S. Abeywickrama, R. Zhang, Q. Wu, and C. Yuen, "Intelligent reflecting surface: Practical phase shift model and beamforming optimizati on," *IEEE Transactions on Communications*, vol. 68, no. 9, pp. 5849-5863, 2020.

[10] D. Xu, X. Yu, Y. Sun, D. W. K. Ng, and R. Schober, "Resource allocation for secure IRS-assisted multiuser MISO systems," in *2019 Globecom Workshops (GC Wkshps)*: IEEE, pp. 1-6.

[11] K. Ansari and M. Majidi, "3D beamforming and secrecy rate improvement in wireless powered communication networks based on intelligent reflecting surfaces," presented at the 11'th Conference on Information and Knowledge Technology (IKT), Tehran, 2020.

[12] M. Hatami and H. Behroozi, "On maximizing the secrecy rate in a cooperative wireless network using friendly jammers," *International Journal of Information and Communication Technology Research*, vol. 8, no. 3, pp. 63-69, 2016.

[13] A. Zakeri and S. M. Razavizadeh, "Securing RIS-aided wireless networks against full duplex active eavesdropping," *International Journal of Information and Communication Technology Research*, vol. 17, no. 1, 2025.

[14] S. R. Shahcheragh and K. Mohamed-Pour, "Beamforming design for simultaneous transmission and reflection reconfigurable intelligent surface assisted secure wireless communication by considering imperfect CSI," *International Journal of Information and Communication Technology Research* vol. 17, no. 2, 2025.

[15] S. K. Moghaddam and S. M. Razavizadeh, "Joint tilt angle adaptation and beamforming in multicell multiuser cellular networks," *Computers & Electrical Engineering*, vol. 61, pp. 195-207, 2017.

[16] S. M. Razavizadeh and T. Svensson, "3D beamforming in reconfigurable intelligent surfaces-assisted wireless communication networks," in *WSA 2020; 24th International ITG Workshop on Smart Antennas*: VDE, pp. 1-5.

[17] S. M. Razavizadeh, M. Ahn, and I. Lee, "Three-dimensional beamforming: A new enabling technology for 5G wireless networks," *IEEE Signal Processing Magazine*, vol. 31, no. 6, pp. 94-101, 2014.

[18] Y.-C. Liang, R. Long, Q. Zhang, J. Chen, H. V. Cheng, and H. Guo, "Large intelligent surface/antennas (LISA): Making reflective radios smart," *Journal of Communications and Information Networks*, vol. 4, no. 2, pp. 40-50, 2019.

[19] M. D. Renzo *et al.*, "Smart radio environments empowered by reconfigurable AI meta-surfaces: An idea whose time has come," *EURASIP Journal on Wireless Communications and Networking*, vol. 2019, no. 1, pp. 1-20, 2019.

[20] Q.-s. Yuan, Y.-j. Hu, C.-l. Wang, and X.-l. Ma, "3D beamforming for improving the security of UAV-enabled mobile relaying system," *Radioengineering*, vol. 28, no. 1, p. 305, 2019.

[21] L. Ge, P. Dong, H. Zhang, J.-B. Wang, and X. You, "Joint beamforming and trajectory optimization for intelligent

[Downloaded from ijict.itrc.ac.ir on 2026-11-11]

reflecting surfaces-assisted UAV communications," *IEEE Access*, vol. 8, pp. 78702-78712, 2020.
[22] Z. Ning *et al.*, "6G communication new paradigm: The integration of unmanned aerial vehicles and intelligent reflecting surfaces," *IEEE Communications Surveys & Tutorials*, 2025, doi: 10.1109/COMST.2025.3526251.
[23] S. Zargari, A. Hakimi, C. Tellambura, and S. Herath, "User scheduling and trajectory optimization for energy-efficient IRS-UAV networks with SWIPT," *IEEE Transactions on Vehicular Technology*, vol. 72, no. 2, pp. 1815-1830, 2022.
[24] S. Li, B. Duo, M. Di Renzo, M. Tao, and X. Yuan, "Robust secure UAV communications with the aid of reconfigurable intelligent surfaces," *IEEE Transactions on Wireless Communications*, vol. 20, no. 10, pp. 6402-6417, 2021.
[25] X. Liu, C. Xie, W. Xie, P. Zhu, and Z. Yang, "Security performance analysis of RIS-assisted UAV wireless communication in industrial IoT," *The Journal of Supercomputing*, vol. 78, no. 4, pp. 5957-5973, 2022.
[26] M. Chai, Y. Liu, S. Zhao, and H. Deng, "Enhancing physical-layer security in UAV-assisted communications: A UAV-mounted reconfigurable intelligent surface scheme for secrecy rate optimization," *Drones*, vol. 9, no. 3, pp. 1-22, 2025.
[27] L. Zhao, S. Qu, H. Xu, Z. Wei, and C. Zhang, "Energy-efficient trajectory design for secure SWIPT systems assisted by UAV-IRS," *Vehicular Communications*, vol. 45, p. 100725, 2024.
[28] Q. Wu and R. Zhang, "Intelligent reflecting surface enhanced wireless network via joint active and passive beamforming," *IEEE Transactions on Wireless Communications*, vol. 18, no. 11, pp. 5394-5409, 2019.
[29] D. Tse and P. Viswanath, *Fundamentals of Wireless Communication*. Cambridge university press, 2005.
[30] L. Zhu, J. Zhang, Z. Xiao, X. Cao, D. O. Wu, and X.-G. Xia, "3-D beamforming for flexible coverage in millimeter-wave UAV communications," *IEEE Wireless Communications Letters*, vol. 8, no. 3, pp. 837-840, 2019.
[31] S. Boyd and L. Vandenberghe, *Convex Optimization*. Cambridge University Press, 2004.



Kosar Ansari received her B.Sc. degree in Electrical Engineering from Isfahan University of Technology and Shahrekord University, Iran, in 2018. She obtained her M.Sc. degree in Telecommunications Engineering from the University of Kashan in 2021. From 2022 to 2024, she worked on PCB design qualification, noise reduction techniques, and PCB simulation. Her research interests include Intelligent Reflecting Surfaces (IRS), beamforming, Wireless Power Transmission (WPT), optimization and secrecy rate.



Mahdi Majidi received the B.Sc. degree in electrical engineering from Isfahan University of Technology, Isfahan, Iran, in 2004, and the M.Sc. and Ph.D. degrees in electrical engineering from Amirkabir University of Technology (Tehran Polytechnic), Tehran, Iran, in 2007 and 2014, respectively. In 2012, he joined the Communications and Networks Laboratory, Department of Electrical and Computer Engineering, National University of Singapore (NUS), Singapore, as a Visiting Ph.D. Student. In 2015, he worked as a researcher at the Iran Telecommunication Research Center (ITRC). Since 2016, he is an assistant professor of the Department of Electrical and Computer Engineering, University of Kashan, Iran. Also, from 2023 to 2024, he worked as a senior communication system designer for the Qualinx BV in the Netherlands. His research interests include numerical and analytical optimization methods, Intelligent reflecting surfaces, machine learning, wireless transceiver design, LPWAN, and localization.

[Downloaded from ijict.itrc.ac.ir on 2026-11-11]